International Journal of Impact Engineering 137 (2020) 103476

Contents lists available at ScienceDirect

International Journal of Impact Engineering

journal homepage: www.elsevier.com/locate/ijimpeng

On the ballistic perforation resistance of additive manufactured AlSi10Mg aluminium plates

Martin Kristoffersen[a,b], Miguel Costas[a,b], Tim Koenis[c], Vegard Brøtan[d], Christian O. Paulsen[b,e], Tore Børvik[a,b,*]

[a] Structural Impact Laboratory (SIMLab), Department of Structural Engineering, Norwegian University of Science and Technology (NTNU), NO-7491 Trondheim, Norway
[b] Centre for Advanced Structural Analysis (CASA), NTNU, NO-7491 Trondheim, Norway
[c] Department of Mechanical Engineering, Eindhoven University of Technology, 5600 MB Eindhoven, the Netherlands
[d] SINTEF Manufacturing AS, NO-7465 Trondheim, Norway
[e] Department of Materials Science and Engineering, NTNU, NO-7491 Trondheim, Norway

ARTICLE INFO

Keywords:
3D printing
Material tests
Bullet impacts
Metallurgical investigations
Finite element simulations

ABSTRACT

Materials and structures made through additive manufacturing (AM) have received a lot of attention lately due to their flexibility and ability to customize structural components of complex geometry. One range of application not exploited so far is the use of additive manufactured metal plates for ballistic protection. In this study, plates of AlSi10Mg with dimensions 100 mm × 80 mm × 5 mm were manufactured in a powder-bed fusion machine. From the printed plates, material specimens were extracted and strained to fracture in uniaxial tension to reveal the mechanical response of the AM material. Metallurgical investigations were also conducted to study the microstructure of the as-built alloy both before and after testing. Next, the perforation resistance of the AM plates was disclosed in a ballistic range. During testing, the plates were impacted by 7.62 mm APM2 bullets at various velocities. In an additional test series, only the hard core of the same bullet inserted in a sabot was fired towards the plates. Based on high-speed camera images, the initial and residual velocities of the different bullets were measured, and the ballistic limit curves and velocities were determined. For comparison, the studies described above were repeated on a traditionally die-cast block of AlSi10Mg having the same chemical composition as the powder used in the 3D printing. Finally, based on the conducted material tests a standard constitutive relation and failure criterion, frequently used in ballistic impact simulations, were calibrated based on inverse modelling. Finite element models of the ballistic impact problems were established in ABAQUS/Explicit, and the numerical results were compared to the experimental data. Good agreement between predicted and experimental results was in general obtained, even though no special measures were undertaken concerning the fact that the target material was additively manufactured.

1. Introduction

In international operations, equipment and personnel are often sent into highly unstable and distant, and sometimes also dysfunctional, regions of the world. A major threat faced in such operations is gunfire from small-arms weapons [1], but it is challenging to know beforehand what level of protection is required. Thus, it is important to be able to repair, strengthen or even re-design the protection locally. One possibility, not really utilized so far, would be to additive manufacture (or 3D print) protective components on site. Even though additive manufacturing allows for a rapid evolution of protective structures [2], there are to the authors' best knowledge no studies in the open literature that address the ballistic perforation resistance of additive manufactured metal plates.

Additive manufacturing (AM) is poised to have a transformational effect in many industries. The successive addition of material is both material efficient and leads to a new paradigm in the freedom of part design. However, while the last few years have seen advances in software and printing technologies, several material-related fundamental challenges remain that hinder the widespread use of additive manufacturing for production. among them are a lack of fully understanding the processing-microstructure-property relationships and the difficulty to rationalize the complex microstructures of AM processed components [2,3]. The changing properties and microstructure stand out as major issues that are hard to cope with in safety critical objects, as one needs to deal with qualification and certification of the parts [4].

* Corresponding author.
E-mail address: tore.borvik@ntnu.no (T. Børvik).

https://doi.org/10.1016/j.ijimpeng.2019.103476
Received 29 September 2019; Received in revised form 3 December 2019; Accepted 10 December 2019
Available online 10 December 2019

Furthermore, due to the nature of the process, the mechanical properties of AM components depend on various factors such as the stock powder material [5], production speed, energy density, build strategy [3], bed heating and the energy required to melt the base material [6,7]. The variation of these factors can dramatically change the microstructure of the material, altering its mechanical properties [8,9]. Also, a series of defects may occur due to falsely chosen parameters, strategy, support or geometric challenges [10].

AM is defined as a process of fabrication where parts are created by adding material, often layer by layer [11]. Powder bed fusion (PBF) is an AM technology which employs a heat source in the form of a laser or electron beam to scan a layer of metal powder, selectively melting the scanned powder to a defined depth into the massive substrate. After the beam passes, the pool of molten metal powder cools down and solidifies, binding the material together [12]. Compared to conventional manufacturing methods such as die-casting, materials produced by laser based PBF experience far greater cooling rates, ranging between 10^3 and 10^{11} K/s [13]. Due to the high cooling rates the material, in this study the aluminium alloy AlSi10Mg, exhibits an extremely fine microstructure consisting of cellular α-phase aluminium dendrites surrounded by a network of eutectic Al-Si. Differences in cooling result in finer Al-dendrites in the centre and coarser Al-dendrites at the border of the melt-pool [14]. The coarse borders of each solidified melt-pool contain larger and more brittle silicon-rich phases. These borders at the outer regions of the melt-pools make the connection between each subsequent layer to act as rather brittle elements [15].

Due to the fine microstructure, AlSi10Mg parts manufactured by laser based PBF generally have higher or comparable mechanical properties as a similar material manufactured by e.g. traditional die-casting [16,17]. AM materials may exhibit some anisotropy, which is expressed in a more brittle mechanical behaviour in the print direction. This is mainly due to the more brittle connection between each subsequent layer [15]. Furthermore, the mechanical properties of printed AlSi10Mg are found to be strain rate sensitive with similar strain rate sensitivity in the print direction and the horizontal directions [18]. However, since the microstructure of the AM material depends on many process parameters and powder properties, there may be large variations in mechanical properties and anisotropy of the material [19].

In this study, aluminium plates of alloy AlSi10Mg with dimensions 100 mm × 80 mm × 5 mm were additive manufactured in a PBF machine. From these plates, a number of material specimens were extracted. The samples were then strained to fracture in uniaxial tension to reveal the mechanical response of the AM material. Metallurgical investigations were also conducted to study the microstructure of the as-built alloy both before and after testing. Next, the perforation resistance of the AM plates was disclosed in SIMLab's ballistic range. During testing, the plates were impacted by 7.62 mm APM2 bullets fired at various velocities from a rifle. In addition, only the hard core of the same bullet inserted in a plastic sabot was fired towards the plates. Based on high-speed camera images, the initial and residual velocities of the different bullets were measured, and the ballistic limit curves and velocities were determined. For comparison, the studies described above were repeated on a traditionally die-cast block of AlSi10Mg having the same chemical composition as the powder used in the 3D printing. No significant difference in ballistic properties between the additive manufactured and the die-cast materials was found. Finally, based on the conducted material tests a standard constitutive relation and failure criterion, frequently used in ballistic impact simulations, were calibrated based on inverse modelling. Finite element models of the ballistic impact problems were established in ABAQUS/Explicit [20], and the numerical results were compared to the experimental data. The agreement between the predicted and the experimental results was in general good, even though no special measures were undertaken concerning the fact that the target material was produced by AM. The finite element simulations gave conservative results, which is desirable from a protective point of view. For comparison, cylindrical cavity expansion approximations were also used to estimate the ballistic limits at a considerably lower computational cost than for the 3D finite element simulations. Again, the results were in reasonable agreement with the experimental findings, but at the non-conservative side of the experimentally obtained ballistic limit curve.

2. Materials

2.1. Material production

Aluminium plates of alloy AlSi10Mg with nominal dimensions 100 mm × 80 mm × 5 mm were additive manufactured using laser beam powder bed fusion (PBF-LB). This is a technology within the group of additive manufacturing (AM) processes. AM describes the fabrication of parts, as the name says, by adding material, often layer-by-layer. In contrast to production by adding material, subtractive manufacturing includes processes like milling, drilling, turning and so on, in which the final shape of a part is achieved by removing material. AM is normally divided into seven categories [21], and PBF is one of such categories with PBF-LB as a specific subcategory. This category describes the process in which a layer of powder is spread on top of a substrate and is thereby selectively melted into a solid. Such melted stacks will grow into a shape that is defined by a CAD model. Building a part layer-by-layer has the advantage of transforming difficult 3D shapes into simple 2D layers that are easier to handle and produce. The material used in this study was delivered through GE Additive under the name CL31AL. This is a DIN EN 1706 AlSi10Mg gas-atomized powder, with a volumetric median diameter of 31.7 μm. The powder has a median HS circularity of 0.76. Thus, the flowability of the powder was well within the optical limits that have been discussed in recent publications [22].

All samples were fabricated in a Concept Laser M2 using a 200 W Yb:YAG fibre laser, where an Argon atmosphere with purity above 99.9% was used as shielding gas. The parts were constructed applying an island scan strategy with an island size of 5 mm × 5 mm. This strategy is a standard Concept Laser strategy to spread the heat input, and hence reduce the build-up of inherent stresses. Therefore, the islands are melted in a randomized order. Furthermore, the islands shift their scan direction 90° at each layer to avoid grooves forming. This strategy also addresses the gaps in between each layer, as the islands are shifted 1 mm in X and Y direction for each layer. This means that every fifth layer is the same. To avoid vibrations and uneven powder distribution from the coater hitting the melt-pools, the islands are rotated 45° with respect to the X-direction (coater direction). An illustration of the printed aluminium plates, giving the position and dimensions of the specimens on the built platform during AM, is shown in Fig. 1.

Several publications in the open literature have shown that preconditioning the aluminium build with an extra laser exposure with lower intensity will increase the density of the parts [23,24]. It is also known that heating of the build platform will in general increase the yield stress and the average fatigue strength. A heating system connected to the substrate was utilized in this study to apply a 200 °C continuous heating. It has been found that the combination of a laser pre-scanning at 50 W and a 200 W main scan at 1400 mm/s yields relative densities above 99.6% [24]. It is also important to note that the hatch spacing was decreased to 97.5 μm compared to the normal 105 μm, and that the layer thickness was kept at 30 μm during the production of the specimens used herein.

A traditionally die-cast AlSi10Mg alloy was also investigated in this work. In order to ensure a comparable microstructure, the chemical composition of the cast material was kept as close as possible to the chemical composition of the AM material. The die-cast material was cast following industrial standards by Hydro Aluminium into a permanent mould having the shape of a horizontal bar with approximate dimensions 75 mm × 53 mm × 600 mm. From this bar, similar

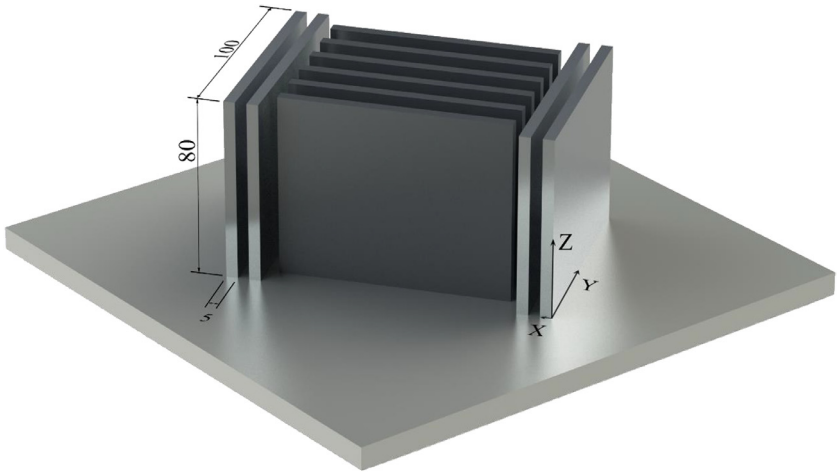

Fig. 1. Position and dimension of the AlSi10Mg plates on the built platform during AM.

Table 1
Chemical composition (in wt%) of the main alloying elements in AlSi10Mg for the AM and die-cast materials.

AlSi10Mg	Si	Fe	Mg	Mn	Ti	Cu	Zn	Al
Printed	9–11	0–0.55	0.2–0.45	0–0.45	0–0.15	0–0.10	0–0.10	Balance
Die-cast	10.623	0.110	0.214	0.0059	0.1274	0.0018	0.0142	88.873

specimens as for the AM material were extracted for further investigations and tests. Table 1 gives the chemical compositions of both the AM and the die-cast materials.

It is also important to note that both the AM and the die-cast materials used in this study were tested in the as-built or as-cast condition, although it is well known that the mechanical properties of the aluminium alloy can be significantly improved by proper heat treatment after production [25–27].

2.2. Metallurgical investigations

The microstructure of both the AM and the die-cast materials was investigated in a Zeiss Ultra 55 Limited Edition Field Emission scanning electron microscope (FE-SEM) and a Leica MEF4M optical microscope (OM). To prepare the specimens for imaging, they were first ground and polished down to 1 μm before a final step to reveal the microstructure was carried out. The final polishing step for SEM imaging and electron backscatter diffraction (EBSD) was based on vibration polishing using a VibroMet2 from Buehler for 12 h and a suspension with pH 8 containing SiO_2 particles with size 0.02 μm. The resulting surfaces were both plane and free of deformations. OM imaging of the pores in the microstructure of the AM and die-cast materials was also conducted on polished specimens. To reveal the microstructure of the materials in the OM, the specimens were anodized after being polished down to 1 μm. The anodizing was performed at 20 V in a HBF_4 solution for 90 s. Finally, all specimens were rinsed in an ultrasonic bath with acetone for 5 min to obtain a clean surface finish.

Fig. 2(a) shows the microstructure of the AM material in all directions, where the print direction is defined as PD (or Z in Fig. 1). These images were acquired by OM using polarized light. The planes in the transverse (TD or Y in Fig. 1) and normal (ND or X in Fig. 1) directions have an almost identical microstructure. This is as expected since each scan track is rotated 90°, showing a front view and a side view of the strings in alternate layers. The built (or PD) plane gives a top view of the strings. Fig. 2(b), showing SEM images of the polished surfaces, reveals several rather large pores in the material. Fig. 2(c) shows EBSD maps revealing the grain structure within the scan tracks. Each map covers an area of 300 μm × 300 μm, obtained using a step-size of 0.5 μm. The colours correspond to a grain orientation given by the legend to the right in the figure. In the PD plane, there is an equiaxed grain structure. On the contrary, the TD and ND planes have elongated grains in the front view of the printed string while the grains are equiaxed in the side view. Fig. 2(d) further illustrates the pore size and density in the AM material based on OM images of polished surfaces. In all planes, a substantial number of pores scattered throughout the surface is seen. The largest pores have diameters of approximately 200 μm in all planes, and the PD plane has several pores of this size.

The die-cast material was investigated in a similar way as the AM material. Fig. 3(a) shows the microstructure of the die-cast material, imaged using OM on a polished specimen. A typical casting microstructure with dendrite arms of aluminium growing in all directions surrounded by a fine eutectic mixture of aluminium and silicon is seen. Here, the cast direction is defined as CD. In Fig. 3(b), EBSD maps giving the grain structure of the die-cast material are shown. The dendrites represent large individual grains, and in between them small equiaxed grains are present. As for the EBSD maps in Fig. 2(b), each colour represents a grain orientation. When studying the cubes in Fig. 3, no significant discrepancies in microstructure between directions were observed. The die-cast material was also investigated for pores. In contrast to the AM material, the die-cast material appeared very dense, with only a few pores. These pores could only be observed in the SEM, because they were quite small, and none of the pores were found to be larger than 2 μm in diameter.

2.3. Material tests setup

Uniaxial tensile tests were performed on axisymmetric smooth specimens taken from different positions and directions in plates of both AM and die-cast materials. The geometry of the test specimens is given in Fig. 4, while Fig. 5 shows the position and direction of the samples. The directions were chosen so that the tensile axis of the specimens was either parallel (0°), diagonal (45°) or normal (90°) with respect to the build or cast direction of the plates.

All tensile tests were carried out at room temperature using a Zwick Roell Z030 universal testing machine with a 30 kN load cell. To have quasi-static loading conditions, the crosshead velocity of the test

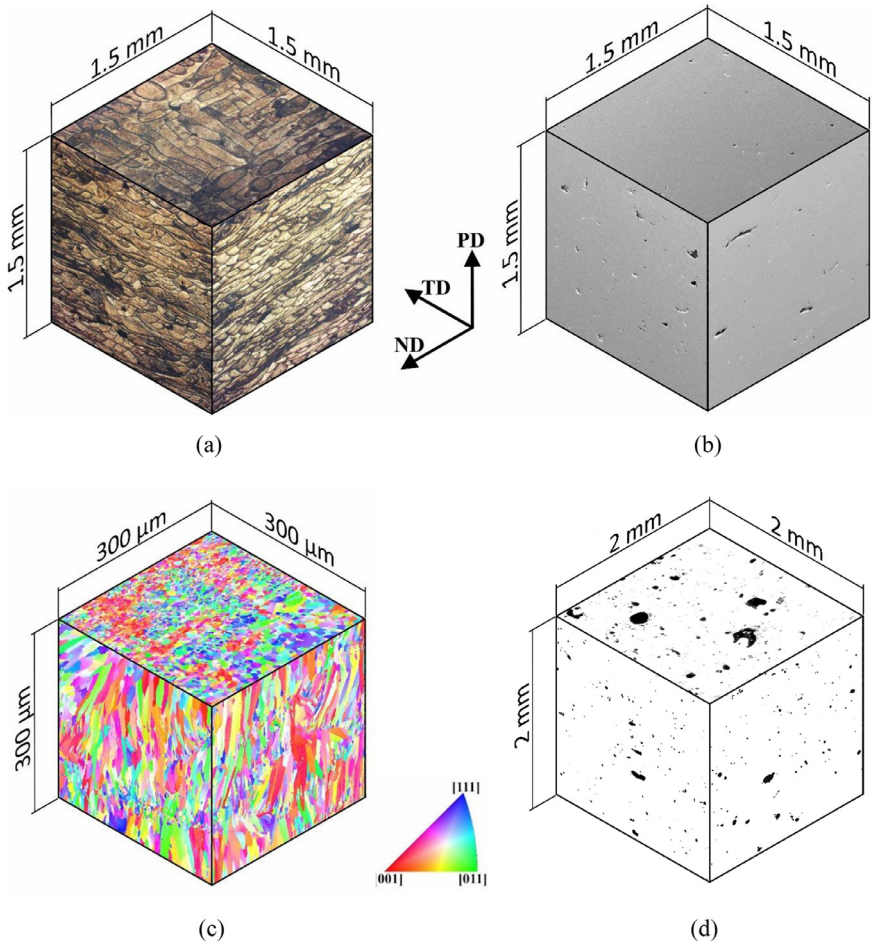

Fig. 2. Cubes illustrating the microstructure of the AM material in different directions. (a) OM images using polarized light on an anodized surface, (b) SEM images of a polished surface, (c) EBSD maps based on SEM images illustrating the grain structure, where each colour is equal to a grain orientation and (d) OM images of the pore size and density.

machine was held constant at 0.15 mm/min, giving an initial strain rate of 5×10^{-4} s^{-1}. During testing, the force and minimum diameter of the specimen in two orthogonal directions were continuously measured until fracture. The force was measured by the calibrated load cell, while the minimum diameter was obtained using a high-speed, contact-less AEROEL XLS13XY laser gauge with 1 µm resolution [28]. The laser gauge creates two perpendicular laser beams, each measuring 13 mm × 0.1 mm, pointing towards detectors on the opposite side of the specimen. To make sure that the minimum cross-section is measured at all times, the laser gauge was installed on a mobile frame free to move vertically. The sample was scanned at a frequency of 1200 Hz during elongation, and the measured data was transferred by the built-in electronics to the remote computer. Before testing, the specimens were adjusted so that the diameters were measured in the thickness (or

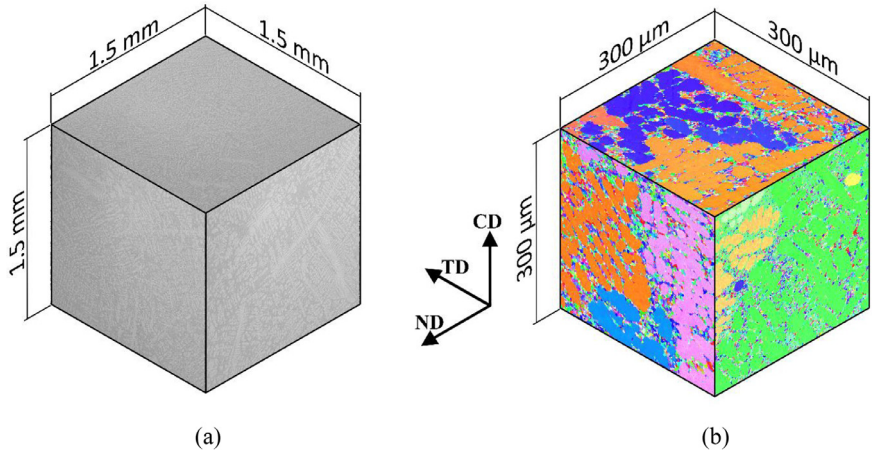

Fig. 3. Cubes illustrating the microstructure of the die-cast material in different direction. (a) OM images of a polished surface and (b) EBSD maps based on SEM images illustrating the grain structure, where each colour is equal to a grain orientation (see Fig. 2(c) for legend).

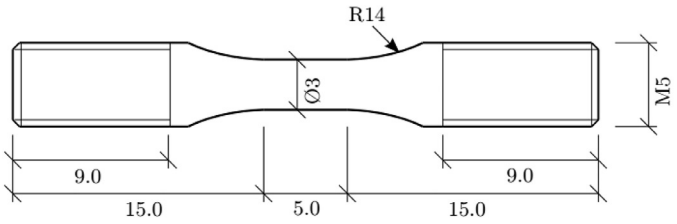

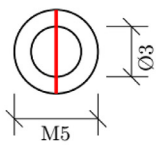

Fig. 4. Geometry of the uniaxial tensile test specimen where the red line gives the thickness direction of the plate (measures in mm).

normal) direction of the plate (D_{ND}) and in the transverse direction of the specimen (D_{TD}), respectively.

The specimens were initially axisymmetric, while the current cross-section area was assumed elliptical. Thus, the initial (A_0) and current (A) cross-section areas can be obtained from the diameter measurements as

$$A_0 = \frac{\pi D_0^2}{4}, \quad A = \frac{\pi D_{ND} D_{TD}}{4} \tag{1}$$

where D_0 is the initial diameter of the specimen. If these areas are combined with the measured force F, the Cauchy (true) stress σ and the logarithmic (true) strain ε can be calculated as

$$\sigma = \frac{F}{A}, \quad \varepsilon = \ln\left(\frac{A_0}{A}\right) = \ln\left(\frac{D_0^2}{D_{ND} D_{TD}}\right) \tag{2}$$

It should finally be noted that small elastic strains and plastic incompressibility are assumed in Eq. (2), and that the calculated Cauchy stress and logarithmic strain are average values across the minimum cross-section area of the specimens. The plastic strain can then be found as $\varepsilon^p = \varepsilon - \sigma/E$, where E is the elastic modulus.

2.4. Material tests results

Obtained Cauchy stress – logarithmic strain curves until fracture based on 12 tensile test specimens taken from an AM plate are shown in Fig. 6, where the stated numbers relate to the specimen numbers given in Fig. 5. Even though the yield stress is rather similar, clear differences in work hardening and strain to fracture are seen depending on the position and direction of the tensile specimen. Specimens 1–4 have their tensile axis oriented 90° to the built direction. However, specimen 1 and 3 are close to the heat platform (holding a constant temperature of 200 °C – see Section 2.1) throughout the complete printing process,

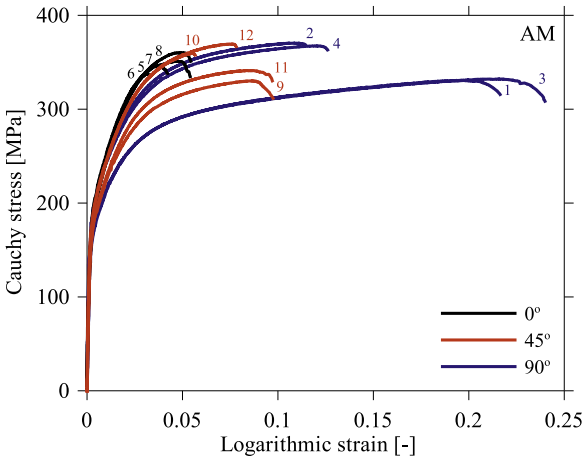

Fig. 6. Cauchy stress – logarithmic strain curves until fracture of tensile test specimens taken from an AM plate. The numbers relate to the specimen number given in Fig. 5.

while specimen 2 and 4 are far from it. Thus, the lower part of the plate close to the build platform will be heat exposed for a much longer time compared to the top of the plate. This continuous heat-treatment has altered the mechanical response of the material, since the flow stress is markedly lower and the strain to fracture markedly higher for specimen 1 and 3 than for specimen 2 and 4. A similar type of response is found for the specimens with tensile axis oriented 45° to the built direction, i.e., specimens 9–12. Here, specimen 9 and 11 are closer to the heat platform than specimen 10 and 12, causing a lower flow stress and a higher fracture strain in the former. Note that the difference is not as distinct as for the specimens oriented 90° to the built direction where the distance, and accordingly the temperature gradient, between the

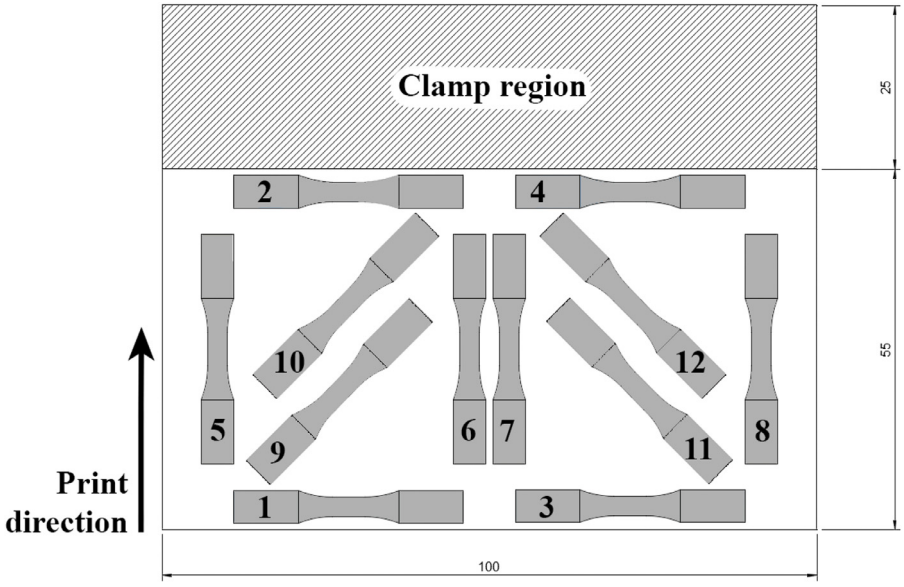

Fig. 5. Position and direction of tensile test specimens in the AM and die-cast plates (measures in mm).

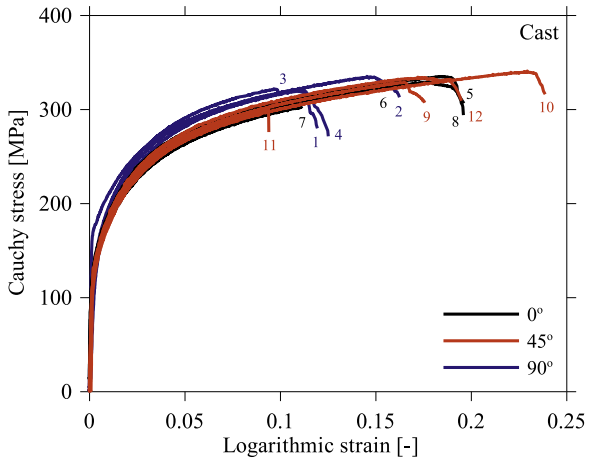

Fig. 7. Cauchy stress – logarithmic strain curves until fracture of tensile test specimens taken from a die-cast plate. The numbers relate to the specimen number given in Fig. 5.

specimens is larger. Finally, specimens 5–8 have their gauge area located at the same distance from the heat platform. Now the flow stress is almost identical for all specimens, while some variation in the fracture strain is still seen. These results illustrate the need for a proper heat-treatment after AM to have more homogeneous mechanical properties [29,30], but this is outside the scope of the present study. Note also that several of the specimens have a fairly low fracture strain, indicating a rather brittle material behaviour.

The material test programme described above was repeated on specimens extracted from a die-cast plate. Fig. 7 shows Cauchy stress – logarithmic strain curves until fracture for the cast material based on the 12 uniaxial tensile tests conducted. As for the AM plate, the numbers in the figure relate to the specimen numbers given in Fig. 5. Here the difference in flow stress is much less than for the AM material, but the scatter in fracture strain is still significant. This is typical for a cast material (see e.g. [31]). The flow stress in specimens with tensile axis oriented 90° to the cast direction is slightly higher than for the other directions. Note also that specimens with tensile axis oriented 45° to the cast direction show both the smallest and largest strain to fracture, with values varying from 0.09 for specimen 11 to 0.24 for specimen 10. This indicates a clear inhomogeneity in the microstructure of the cast alloy, probably due to the large grains seen in Fig. 3(b). In general, the flow stress is found to be lower and the fracture strain seems to be higher for the cast material compared to the AM material.

The fracture surface of specimen 3 from the AM plate is shown in Fig. 8. Here, Fig. 8(a) gives an overview of the total area, while Fig. 8(b) illustrates the dimple structure acquired within the white circle marked in Fig. 8(a). The dimple structure indicates a ductile fracture, which is also supported by the tensile curve in Fig. 6. Note that specimen 3 is the most ductile specimen for the AM material with a fracture strain of roughly 0.24. A large crack is also seen inside the red circle of Fig. 8(a). This crack, along with several other smaller cracks observed throughout the fracture surface, unquestionably reduces the ductility of the specimen. These cracks are also consistent with the observations of pores in Fig. 2.

In addition to the obvious heat-platform effect, a rather distinct anisotropic response with specimen orientation on both the flow stress and the strain to fracture is seen from Figs. 6 and 7. The Lankford coefficient (r-ratio) is a measure of the plastic anisotropy of a material and is given as the ratio between the incremental strain in the transverse direction (TD) of the specimen and the incremental strain in the thickness direction (ND) of the plate. Both these strains are continuously measured by the laser gauge described in Section 2.3, and acquired values are given in Table 2. The r-ratios of the AM material are as expected, indicating that the degree of anisotropy is highest in specimens less affected by the heat source. For the die-cast material, the r-ratios show no clear coherence. This may be due to the ratio between the diameter of the test sample and the grain size of the cast material being much less than the corresponding ratio for the AM material, making these measurements highly uncertain. Similarly, the flow stress ratio (R-ratio) gives the anisotropy in flow stress of the material. It is usually defined as the yield stress in a rotated direction relative to a reference direction (e.g. the built or the cast direction). In this study, the R-ratios are close to unity if the flow stress is based on the 0.2% proof stress in the different directions but seems to decrease with plastic straining for the AM material, signifying that the work hardening is anisotropic. However, the possible effects of plastic anisotropy in the materials will not be studied any further in the following and are left for further work.

3. Component tests

3.1. Experimental set-up

The ballistic tests were carried out in a compressed gas gun facility described in detail in Børvik et al. [1,32,33]. In this study, a 7.62 × 63 mm specially designed smooth-bored Mauser gun with a barrel length of 1 m was used to fire the bullets. During testing, the stock was removed, and the rifle was mounted in a rigid rack inside a 16 m^3 impact chamber to guarantee a well-defined impact point for each test. The rifle was fired by a magnetic trigger from safe distance. A sabot trap located just in front of the rifle was used to suppress muzzle flames, since the distance from the rifle muzzle to the target plate was

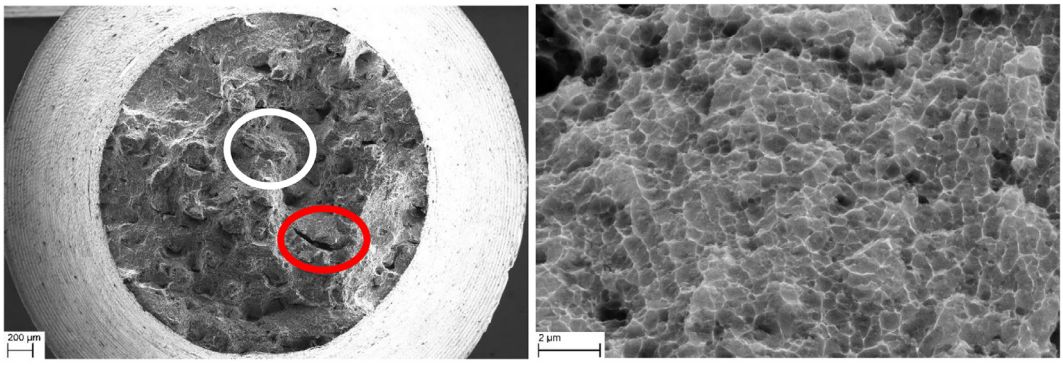

Fig. 8. Fracture surface of a typical tensile test specimen showing (a) an overview and (b) a higher magnification from inside the white circle showing a dimpled fracture surface. A large crack is seen inside the red circle in (a). This specimen corresponds to specimen 3 in Fig. 5.

Table 2
Measured Lankford coefficients (r-ratios) from AM and die-cast materials.

AlSi10Mg	Specimen number											
	1	2	3	4	5	6	7	8	9	10	11	12
AM	0.71	0.50	0.69	0.49	0.94	1.03	0.94	0.91	0.76	0.73	0.74	0.74
Die-cast	0.94	0.80	1.16	1.04	0.84	1.36	1.25	1.12	1.82	0.87	1.25	0.79

not more than 0.6 m. Before testing, the hole in the sabot trap was covered with a break-wire trigger plate used to activate the Phantom v2511 high-speed camera and the flashlights. The high-speed camera was operated at a recording rate of 100,000 fps and used both for visualization of the perforation process and for velocity measurements.

Target plates with dimensions 100 mm × 80 mm × 5 mm of either AM or die-cast materials were firmly clamped along one long side (with a bite of 25 mm – see Fig. 5 for the clamp region) and adjusted to the desired point of impact. This secured a fixed boundary of one of the vertical sides of the plate, while the others remained free. Thus, the boundary conditions during testing were well defined even though not fully clamped. It is however believed that the boundary conditions are of minor importance in high-velocity ballistic impacts if the in-plane distance between single shots and the boundary is more than a few projectile diameters [1]. Here, the nominal in-plane distance between each shot and the boundary was 25 mm in the vertical direction, and 27.5 mm in the horizontal direction. This means that the shots were placed at the same location in the plates as the centre of the gauge area of tensile test specimens 5–8. A maximum of 3 shots were allowed in each target plate before it was replaced. Before testing, the thickness of the plates was measured by a precision calliper and found to be 5.3 mm, i.e., somewhat thicker than the nominal value.

Before each test, the ammunition was adjusted to a predefined velocity. This was done using adjustment graphs, relating the amount of powder in the cartridge to the measured muzzle speed of the bullet. The AP bullet consists of a brass jacket, a lead cap, an end cap and a hardened steel core as shown in Fig. 9 [34,35]. The mass of the hardened steel core is 5 ± 0.25 g, while the mass of the whole bullet is 10.5 ± 0.25 g. First, AP bullets were used in 6 shots against two AM plates and 9 shots against three die-cast plates (i.e., 3 shots in each plate). Second, the test series described above was repeated using the hard core only (CO) of the AP bullet to impact the target plates. In this case, the 6.1 mm diameter hard steel core was encased in a 0.3 g plastic sabot before being inserted into the adjusted cartridge. It is assumed that the hardened steel core, having a Rockwell C hardness of 63, is not plastically deformed during impact with the much softer target plate. In total 30 ballistic impact tests were carried out using the experimental set-up described above.

3.2. Experimental results

Figs. 10 and 11 show typical high-speed camera images of the perforation process of an AM AlSi10Mg aluminium plate impacted by an AP bullet and a CO bullet, respectively, while Figs. 12 and 13 show corresponding images from tests on a die-cast AlSi10Mg target plate. From these images, some interesting observations are made. First, in all cases the bullet perforates the plate by ductile hole growth with limited fragmentation. A few fragments are as seen ejected from the target plates, but not more than what is normally observed for other ductile materials [36,37]. Petals are formed on both sides of the penetration channel, and the perforation process appears more ductile than expected. However, when comparing Fig. 10 with Fig. 12, i.e., perforation of an AM plate and a die-cast plate by an AP bullet, the petals are more distinct for the die-cast plate in that particular test. This may be due to the in general higher ductility of the die-cast alloy (see also Figs. 6 and 7). Second, the bullets are seemingly not deformed during the perforation process, and the brass jacket is still intact and not ripped off the core as it normally is when perforating high-strength targets (e.g. [37]). This may affect the cavity expansion, as more material must be moved away laterally for the AP bullet to pass than for the CO bullet. The pitch of the bullet was in general low, and below 3° in all tests. Finally, some bending of the target plate, especially at the lowest impact velocities, was detected. This is mainly caused by the boundary conditions, since the plates were only clamped along one side (see Fig. 5). It was also found hard to adjust the ammunition to velocities below 300 m/s, and at the same time maintain a straight flight path, due to the lack of gyroscopical stabilization (i.e., spin) of the bullet.

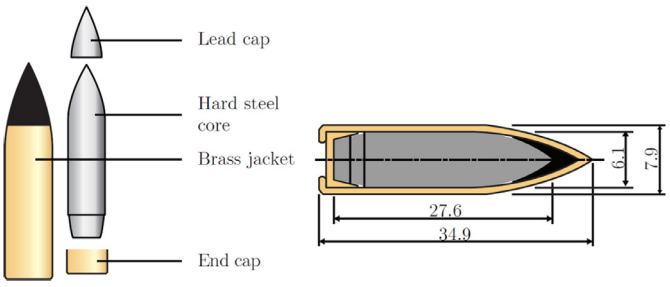

Fig. 9. AP bullet used in tests (measures in mm).

A ROMER Absolute Arm 7252SI, consisting of a probe and a laser scanner, was used to scan the plates after perforation. The probe was used to define the coordinate axes, while the laser was used to scan the plates. The data were processed by the software PC-DMIS and exported as point clouds and stereo-lithographic files. Fig. 14 shows a typical 3D scan of an AM plate perforated by three AP bullets having impact velocities between 450 and 900 m/s. The ductile appearance with multiple petals on both sides of the penetration channel is clearly seen. Similar responses were seen for the other tests, so these scans are omitted for brevity.

Measured initial versus residual velocity curves for AM and die-cast AlSi10Mg plates impacted by AP bullets are given in Fig. 15, while corresponding results for CO bullets are shown in Fig. 16. The solid lines through the experimental data points are based on a best fit to a generalized Recht–Ipson (RI) model. This model has shown to give excellent agreement with experimental data in similar impact studies (see e.g. [1,32,35]). As it was hard to determine the ballistic limit velocities experimentally due to the rather low capacity of these target plates, they were estimated using the RI-model. It is given as [38]

$$v_r = a(v_i^p - v_{bl}^p)^{1/p} \tag{3}$$

where v_i and v_r are the measured initial and residual velocities of the bullet, respectively, while v_{bl} is the sought ballistic limit velocity. Based on conservation of energy and momentum it can be shown that $a = m_p/(m_p + m_{pl})$ and $p = 2$, where m_p is the mass of the projectile and m_{pl} is the total mass of possible plugs or fragments. Note also that a and p may be considered as empirical constants. Since the projectile perforated the targets with limited fragmentation, it was decided to keep $a = 1$ and $p = 2$ in this study, and only fit the ballistic limit velocity v_{bl} to the experimental data using the method of least squares. Based on this approach, the ballistic limit velocities for all configurations were obtained and the results are given in Table 3.

Both Figs. 15 and 16 show that the fitted ballistic limit curves are

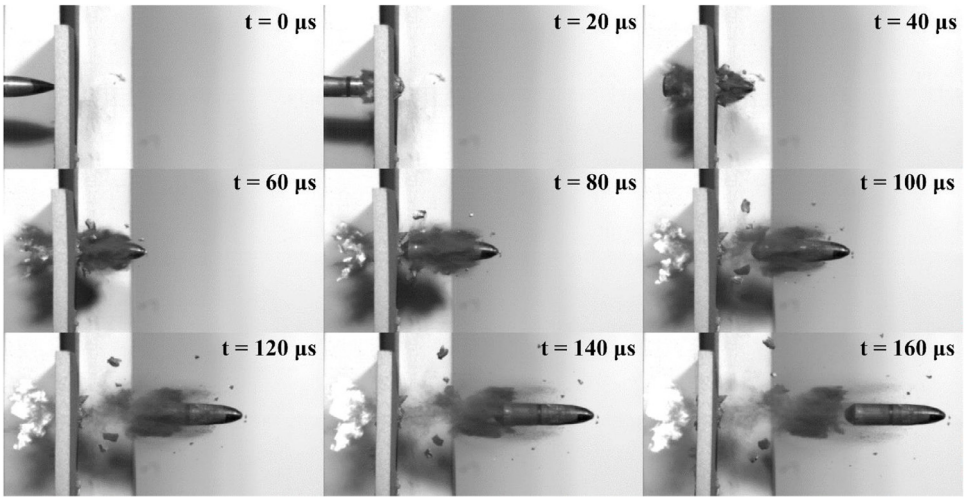

Fig. 10. High-speed camera images versus time showing an AP bullet perforating a 5 mm thick AM AlSi10Mg plate (v_i = 606.2 m/s, v_r = 564.8 m/s).

almost perfectly on top of each other, indicating that the ballistic perforation resistance is identical for an AM and a die-cast AlSi10Mg target plate. This conclusion is valid for both bullet types. From the estimated ballistic limit velocities given in Table 3, it is suggested that the capacity is slightly higher for the AM plate than for the die-cast plate, but the difference is minor. It is also found that the ballistic limit velocity is slightly higher for an AP bullet than for a CO bullet. This contrasts with earlier observations [34,39], where the ballistic limit velocity has been found to be about 10% lower for AP bullets than for CO bullets. The reason for this seems to be that in the earlier studies the jacket was stripped from the core of the AP bullet by the target, while in this study the AP bullet was intact after perforation. Thus, a wider perforation channel, demanding more plastic work, is required. However, the difference in ballistic limit between AP and CO bullets was not more than 3–4%. In any case, the very important conclusion from these tests is that an AM material may have similar or even better ballistic properties than a traditionally manufactured material with the same chemical composition.

The fracture surfaces along the central part of the penetration channel for AM plates perforated by AP or CO bullets are given in Fig. 17. In both images, the bullet enters at the top of the picture and exits at the bottom. The penetration channel left by the AP bullet is as seen smooth close to the entrance, while closer to the exit it leaves a rough surface. In contrast, the CO bullet leaves a rough surface throughout the whole penetration channel. Nonetheless, the penetration channels appear similar and ductile with no visible internal cracks.

4. Material model

4.1. Constitutive relation and failure criterion

In the following, a material model frequently used in numerical simulations of ballistic impact will be applied in an attempt to predict the behaviour of the AlSi10Mg target plates during ballistic impact. Only the AM material will be modelled in this study, since the as-built and as-cast plates showed an almost identical response in the shooting tests. The material behaviour is described by an elastic-thermo-viscoplastic model assuming an elastic modulus of 70 GPa and a Poisson's ratio of 0.3, which are typical values for aluminium found in the literature. A modified version of the Johnson–Cook constitutive model was assumed for the thermoviscoplastic part, where plasticity is defined by the Hershey yield criterion with an exponent equal to 8, the associated flow rule, and a constitutive relation given as [40,41]

$$\sigma_{eq} = (\sigma_0 + R(p))(1 + \dot{p}^*)^C(1 - T^{*m}) \quad (4)$$

Here, σ_{eq} is the Hershey equivalent stress, σ_0 is the yield stress, R is the isotropic hardening variable, p is the equivalent plastic strain, $\dot{p}^* = \dot{p}/\dot{p}_0$ is a dimensionless plastic strain rate, and $\dot{p}_0$ is a user-defined reference strain rate. The homologous temperature is given as

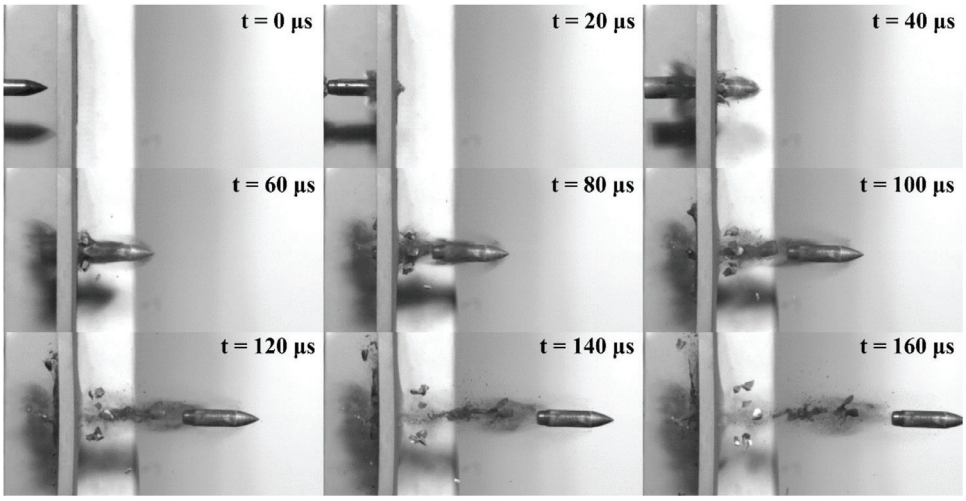

Fig. 11. High-speed camera images versus time showing a CO bullet perforating a 5 mm thick AM AlSi10Mg plate (v_i = 663.5 m/s, v_r = 619.7 m/s).

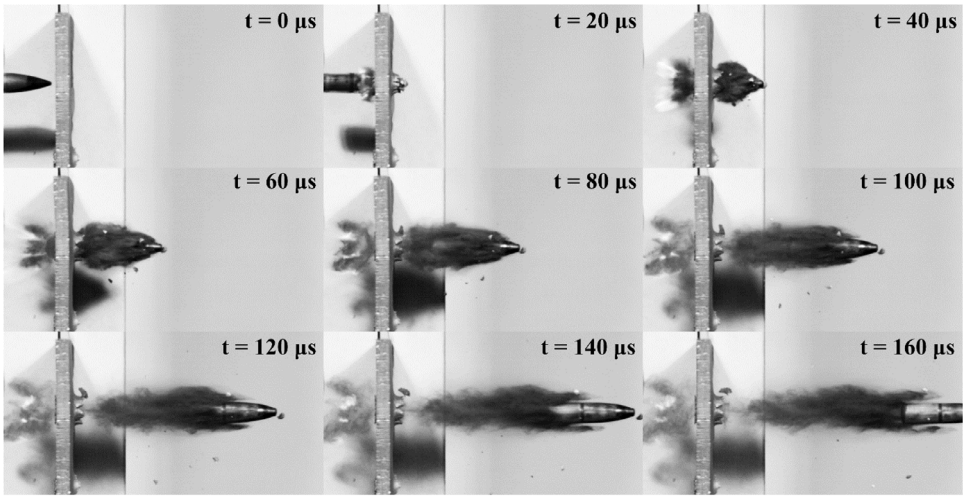

Fig. 12. High-speed camera images versus time showing an AP bullet perforating a 5 mm thick die-cast AlSi10Mg plate ($\boldsymbol{v_i}$ = 737.9 m/s, $\boldsymbol{v_r}$ = 703.7 m/s).

$T^* = (T - T_r)/(T_m - T_r)$, where T is the actual temperature, T_r is the ambient temperature and T_m is the melting temperature of the material. The model parameters C and m govern the strain rate sensitivity and thermal softening of the material, respectively. The isotropic hardening is defined by an extended Voce hardening rule on the form

$$R(p) = \sum_{i=1}^{3} R_i(p) = \sum_{i=1}^{3} Q_i\left(1 - \exp\left(-\frac{\theta_i}{Q_i}p\right)\right) \tag{5}$$

where R_i are hardening terms that saturate at different levels of plastic strain, and the hardening parameters Q_i and θ_i represent the saturation value and the rate of saturation of the hardening term R_i, respectively. The change in temperature due to adiabatic heating is calculated as

$$\dot{T} = \frac{\chi}{\rho c_p}\sigma_{eq}\dot{p} \tag{6}$$

where ρ is the density, c_p is the specific heat and χ is the Taylor–Quinney coefficient. The Taylor–Quinney coefficient is usually taken as 0.9, assuming that 90% of the plastic work is dissipated as heat while the rest is stored in the material as strain energy.

Ductile failure is modelled by the uncoupled damage evolution rule proposed by Cockcroft and Latham [42], which reads

$$D = \frac{1}{W_c}\int_0^p \langle \sigma_I \rangle \, dp = \frac{1}{W_c}\int_0^p \left\langle \sigma^* + \frac{3 - L}{3\sqrt{3 + L^2}} \right\rangle \sigma_{eq}^{vM} \, dp \leq 1 \tag{7}$$

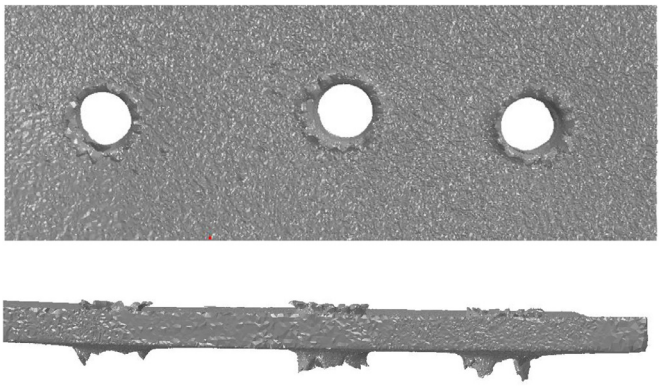

Fig. 14. 3D scan of an AM plate perforated by AP bullets seen from the front (top) and the side (bottom). Note that the images have been cropped to better show the details.

where D is the damage variable, W_c is the failure parameter, σ_I is the major principal stress and $\langle \cdot \rangle$ are the Macaulay brackets defined as $\langle x \rangle = \max(x, 0)$. According to the Cockcroft–Latham criterion, damage only evolves for tensile stresses and is driven by the plastic work amplified by a factor depending on the stress state. Failure occurs when D reaches unity. In the definition of the damage variable, the major

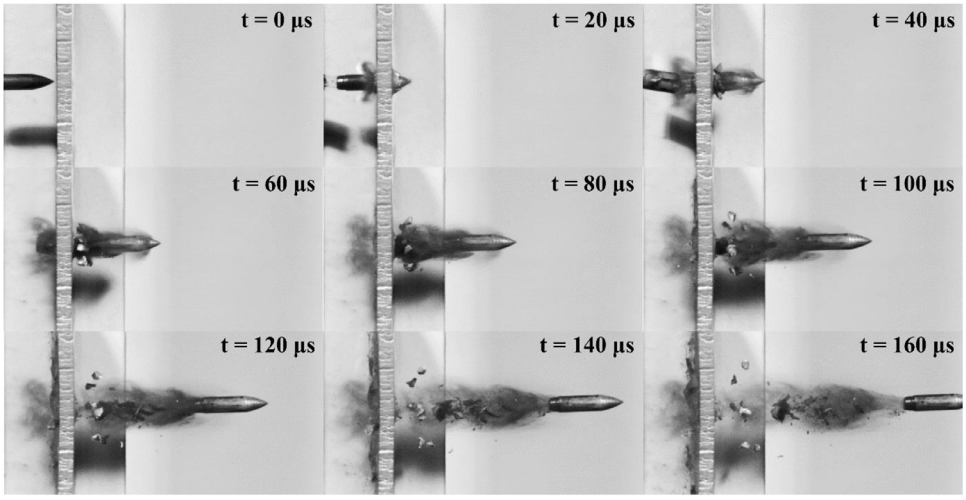

Fig. 13. High-speed camera images versus time showing a CO bullet perforating a 5 mm thick die-cast AlSi10Mg plate ($\boldsymbol{v_i}$ = 694.1 m/s, $\boldsymbol{v_r}$ = 655.0 m/s).

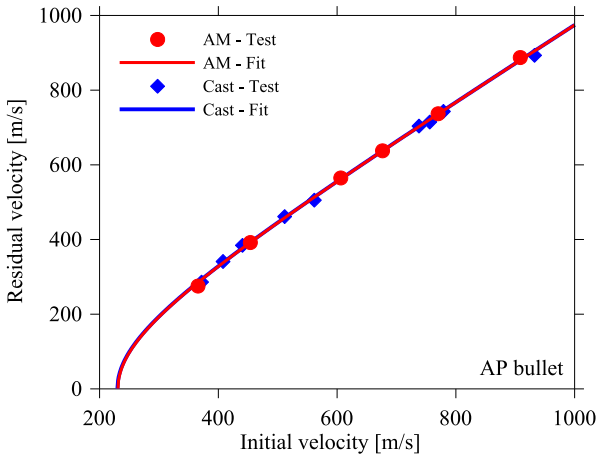

Fig. 15. Initial versus residual velocity curves for AM and die-cast AlSi10Mg plates impacted by AP bullets. The solid lines through the experimental data points are based on a best fit to the Recht–Ipson model.

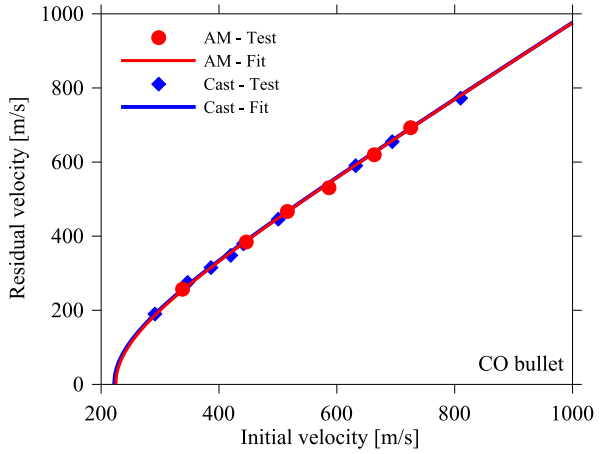

Fig. 16. Initial versus residual velocity curves for AM and die-cast AlSi10Mg plates impacted by CO bullets. The solid lines through the experimental data points are based on a best fit to the Recht–Ipson model.

Table 3
Recht–Ipson constants (a and p) and ballistic limit velocities (v_{bl}) for AM and die-cast AlSi10Mg plates impacted by AP bullets and CO bullets.

AlSi10Mg	AP bullets			CO bullets		
	a	p	v_{bl} [m/s]	a	p	v_{bl} [m/s]
AM	1	2	231.6	1	2	225.5
Die-cast	1	2	230.7	1	2	222.9

principal stress σ_I in Eq. (7) is expressed in terms of the von Mises equivalent stress σ_{eq}^{vM}, the stress triaxiality σ^* and the Lode parameter L, where the latter two stress invariants are defined by

$$\sigma^* = \frac{\sigma_H}{\sigma_{eq}}, \quad L = \frac{2\sigma_{II} - \sigma_I - \sigma_{III}}{\sigma_I - \sigma_{III}} \tag{8}$$

where $\sigma_I \geq \sigma_{II} \geq \sigma_{III}$ are the ordered principal stresses and $\sigma_H = (\sigma_I + \sigma_{II} + \sigma_{III})/3$ is the hydrostatic stress. The robustness of the CL criterion has been proven in e.g. [1,37] and [43].

4.2. Calibration of material constants

The work-hardening parameters in Eq. (5) and the Cockcroft–Latham failure parameter in Eq. (7) were calibrated based on inverse modelling of the tensile tests. The tensile specimen depicted in Fig. 4 was modelled in ABAQUS/Standard [20] using a refined mesh of axisymmetric elements with an approximate element size of 0.075 mm and applying the same loading conditions as those in the experimental tensile tests. An optimization algorithm run under LS-OPT [44] provided the set of parameters θ_i and Q_i which gave the optimal fit of the hardening model to the experimental engineering stress versus diameter reduction curves. It is worth mentioning here that the diameter of the specimen in the finite element model was compared against an equivalent experimental diameter D_{eq} computed as $D_{eq} = \sqrt{D_{ND} D_{TD}}$, where D_{ND} and D_{TD} are the diameters measured by the laser gauge in two orthogonal directions. The fit was performed using the experimental data for three different directions, namely 0° (specimen 8), 45° (specimen 11) and 90° (specimen 1) with respect to the built direction (PD), resulting in the optimal sets of hardening parameters provided in Table 4.

A similar strategy was used for the calibration of the Cockcroft–Latham failure parameter W_c. The tensile specimen was remodelled using the same element type and size as in the subsequent impact simulations (see Section 5.1), i.e., 8-node linear solid elements with reduced integration and an element size of 0.10 mm. The simulations were stopped at the same displacement as failure in the corresponding experiment, and the failure parameter was found by numerical integration of Eq. (7) when $D = 1$ using information from the centremost (critical) element. In this way, the values presented in Table 4 were obtained, which show a strong variation in ductility with orientation. This is in line with the experimental observations, as shown in Fig. 6. The measured force – diameter reduction curves and the calculated Cauchy stress – logarithmic strain curves from the experimental tests until failure are compared with the fitted curves based on the optimization in Fig. 18, showing excellent correlation. Note that failure is here defined as the logarithmic stain at the maximum Cauchy stress.

Since no tests at elevated strain rates or temperatures were conducted, the value of the viscosity and thermal parameters in Eq. (4) were taken from the literature [35], with values $C = 0.001$, $\dot{p}_0 = 5 \times 10^{-4}\ s^{-1}$, $T_m = 893\ K$, $T_0 = 293\ K$ and $m = 1$. The customary value of 0.9 was adopted for the Taylor–Quinney coefficient, and the specific heat was taken equal to 910 J/kgK. Material data for the different parts of the AP bullet were taken from Børvik et al. [1], and are given in Table 5 for completeness. A yield exponent equal to 2 was used for the bullet, thus reducing the Hershey yield criterion to the von Mises yield criterion.

5. Computational approach

5.1. Finite element model

All impact simulations were run using the finite element solver ABAQUS/Explicit [20]. Similar to the calibration of the failure parameter W_c, all parts were discretized by 8-node linear solid elements with reduced integration and stiffness-based hourglass control. The material model as described in Section 4 was used to represent the target plate and all materials in the AP bullet. Material parameters are given in Table 4 for the AM target plate and in Table 5 for the bullet. Simulations were run using material parameter sets from all three calibrations (0°, 45° and 90° in Table 4) to investigate their effects on the estimated ballistic limit curve.

The target plate was clamped in the tests, but in the simulations the boundary conditions were slightly simplified. Only the exposed area of the plate, measuring 55 mm × 100 mm (see Fig. 5), was modelled. This means that the bite area for the clamp was replaced by restraints on the nodes on the face towards the clamping end as illustrated in Fig. 19. This should not affect the results to any significant extent because the deformations in the plates are very local as seen in Fig. 14. The plate thickness was modelled as measured by a precision calliper, i.e.,

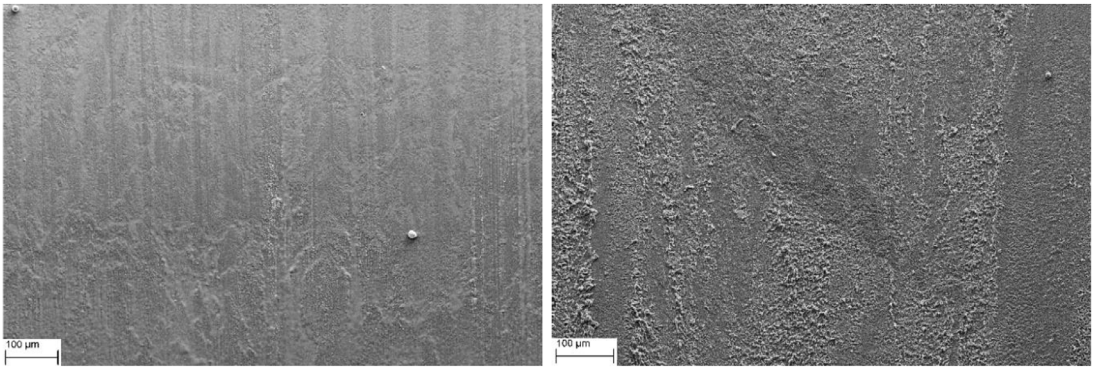

Fig. 17. Fracture surfaces along the central part of the penetration channel for AM plates perforated by (a) an AP bullet and (b) a CO bullet.

Table 4
Work-hardening and failure parameters of AM AlSi10Mg fitted to the experimental tensile data in three different orientations (given in MPa). The orientations are given with respect to the built direction.

Orientation	σ_0	Q_1	θ_1	Q_2	θ_2	Q_3	θ_3	W_c
0°	150	18.61	28,240	204.8	12,900	1.05	67.26	13.7
45°	150	9.68	6310	178.8	10,490	12.24	11.11	26.5
90°	130	43.63	106,000	125.6	6256	43.23	135.5	58.3

5.3 mm. The element size of the centre part of the plate, measuring 16 mm × 16 mm, was about 0.1 mm. A mesh transition zone was made just outside this area to change the number of elements across the thickness from 54 to 18 (i.e., from 0.1 mm to 0.3 mm). Along the plate boundaries, the element length is 0.60 mm. In total, the plate consisted of approximately 3.2 million elements while the bullet was discretized by approximately 10,000 elements. Simulations using both the AP and the CO bullets were carried out. Frictionless contact was enforced between all parts using the general contact algorithm in ABAQUS/Explicit [20], with each surface pair defined including self-contact. A frictionless contact was chosen because it ensures conservative results, and the effect of friction in high-velocity ballistic impact is considered low [1]. The internal surfaces were included in the contact detection to account for new contact surfaces due to element erosion. All parts were given an initial temperature of 293 K (room temperature), and the bullet was given an initial velocity v_0. A final validation case was run whereby one plate was perforated by three AP bullet, like in the experiments. For these simulations, the three penetration areas were created with a refined mesh like in Fig. 19. This mesh was made up of approximately 8.7 million elements.

It should finally be noted that numerical simulations of ballistic impact, involving strain softening due to adiabatic heating, are highly mesh-size dependent (see e.g. [45]). In this study, the thermo-viscoplastic constitutive relation defined in Eq. (4), including both strain-rate hardening and thermal softening, is adopted. Adding viscoplasticity is known to regularize finite element solutions of strain-softening materials, but it is important to keep in mind that viscoplasticity alone does not remove the mesh dependency [46]. A pragmatic way of circumventing the mesh dependency is to apply the computational cell approach [47]. In this approach, a characteristic element size that is sufficiently small to describe the mechanical behaviour of the material and sufficiently large to make reasonable simulations of the actual problem is chosen. Here, a characteristic element size of 0.1 mm was applied both in the calibration of the failure criterion and in the ballistic impact tests. Thus, a mesh sensitivity study is deemed unnecessary.

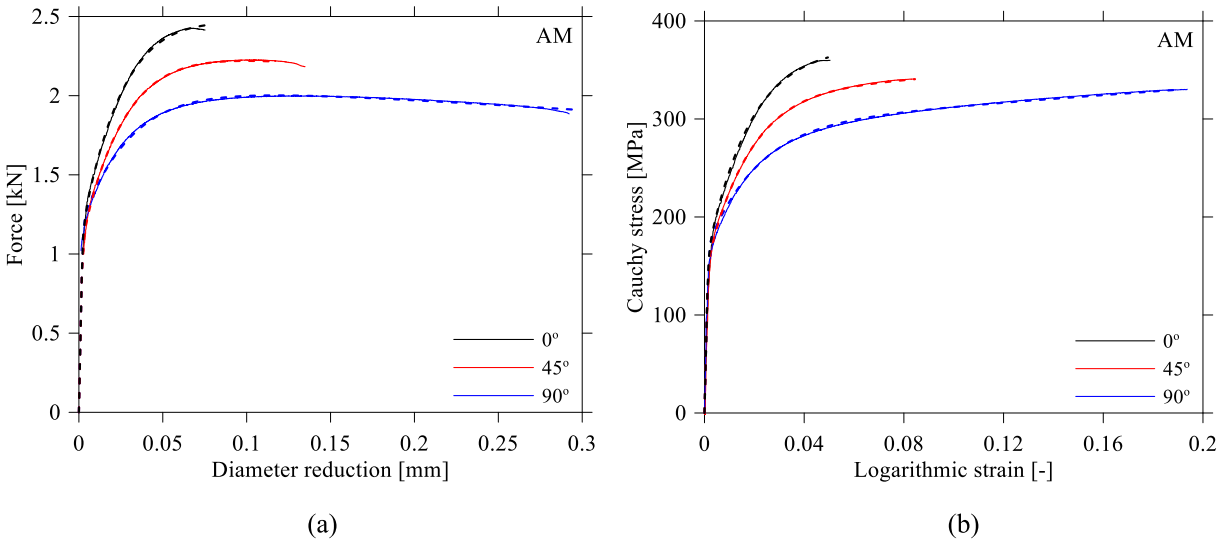

Fig. 18. (a) Force – diameter reduction curves and (b) Cauchy stress – logarithmic strain curves from representative tensile tests and the calibration of the constitutive relation in different built directions. The curves are plotted to failure, defined as the logarithmic strain at maximum Cauchy stress. The solid lines show the experimental curves, while the dotted lines show the fitted curves.

Table 5
Material constants for the APM2 bullets used in the MJC constitutive relation and CL fracture criterion [1].

Material	E [MPa]	ν	ρ [kg/m^3]	c_p [J/kgK]	χ	α [K^{-1}]	T_c^*
Hardened steel core	210,000	0.33	7850	452	0.9	1.2×10^{-5}	0.9
Lead cap	10,000	0.42	10,660	124	0.9	2.9×10^{-5}	0.9
Brass jacket	115,000	0.31	8520	385	0.9	1.9×10^{-5}	0.9

	Yield stress	Strain hardening		Strain rate hardening		Temperature softening			CL
	A [MPa]	B [MPa]	n	$\dot{\varepsilon}_0$ [s^{-1}]	C	T_r [K]	T_m[K]	m	W_c [MPa]
Hardened steel core	1200	50,000	1.0	5×10^{-4}	0	293	1800	1.0	–
Lead cap	24	300	1.0	5×10^{-4}	0.1	293	760	1.0	175
Brass jacket	206	505	0.42	5×10^{-4}	0.01	293	1189	1.68	914

5.2. Finite element results

The CPU time was very dependent on the bullet type and calibration used. For the CO bullet and the 0° calibration, the average time per CPU per simulated μs was approximately 2100 s, while for the 90° calibration it was 5200 s. This result is caused by the higher value of W_c, which allows for more distorted elements and thus a reduced critical time step. The 45° calibration was closer to the 0° calibration, with an average time of about 2500 s per CPU per simulated μs. For the AP bullet, the CPU time was roughly doubled.

Fig. 20(a) shows the ballistic limit curves for the AP bullet based on the three different calibrations, while Fig. 20(b) shows corresponding curves for the CO bullet. The 0° calibration (resulting in the highest strength and the lowest strain to failure according to Fig. 18) gives the lowest estimated ballistic limit, while the 90° calibration (resulting in the lowest strength and the largest strain to failure according to Fig. 18) gives the highest estimated ballistic limit for both bullet types. Thus, ductility seems to increase the perforation resistance more than strength in these simulations. The 90° calibration also gives the predictions closest to the experimental findings. The difference between the calibrations diminishes with increasing initial velocity in line with established knowledge. Note also that all the estimated curves are on the conservative side of the experimental curve (see Fig. 20), and that they in general provide reasonable predictions. The predicted ballistic limit velocities are roughly 15–25% lower than the corresponding experimental value when the simulations are based on the calibration in the 90° direction. The fact that the simulations are conservative, no matter which calibration used, is an important result from a protective point of view. Note also that simulations using the AP bullet give more conservative results, and that the scatter in ballistic limit curves between the different calibrations are generally less than in corresponding simulations using the CO bullet. However, the difference in results between AP and CO bullets are in this study found to be minor, both in tests and simulations, and the cores are seemingly undeformed after perforation. This indicates that similar results would have been obtained if the bullet was modelled as a rigid body for simplicity, but this is not always the case.

Aside from giving quantitatively different results in terms of ballistic limit velocities, the various calibrations also gave rise to distinct qualitative differences in the target response. Fig. 21 illustrates these differences by showing a simulated cross-section of the plate for each calibration during perforation (35 μs after initial contact) by either an AP bullet or a CO bullet with an initial velocity $v_i = 700$ m/s. For the 0° calibration, Fig. 21(a) and (d) show that the bullet mainly erodes its way through the plate due to the rather low W_c (see Table 4), but with some cracking and fragmentation for the AP bullet. The response is similar for the 45° calibration shown in Fig. 21(b) and (e), but here higher values of plastic strain are attained. In Fig. 21(c) and (f), the 90° calibration is seen to produce both petalling and fragmentation, fully in line with the experimental results (see e.g. Fig. 11). It is also observed that the plastic zone is extended to a larger volume of the plate for this calibration, thus absorbing more energy (and thereby increasing the ballistic limit). Still, the deformation of the plate is considered local. Note finally that in a similar way as in the experiments, the jacket is not ripped of the AP bullets in these simulations. For higher strength materials, the jacket is normally ripped of the bullet both experimentally

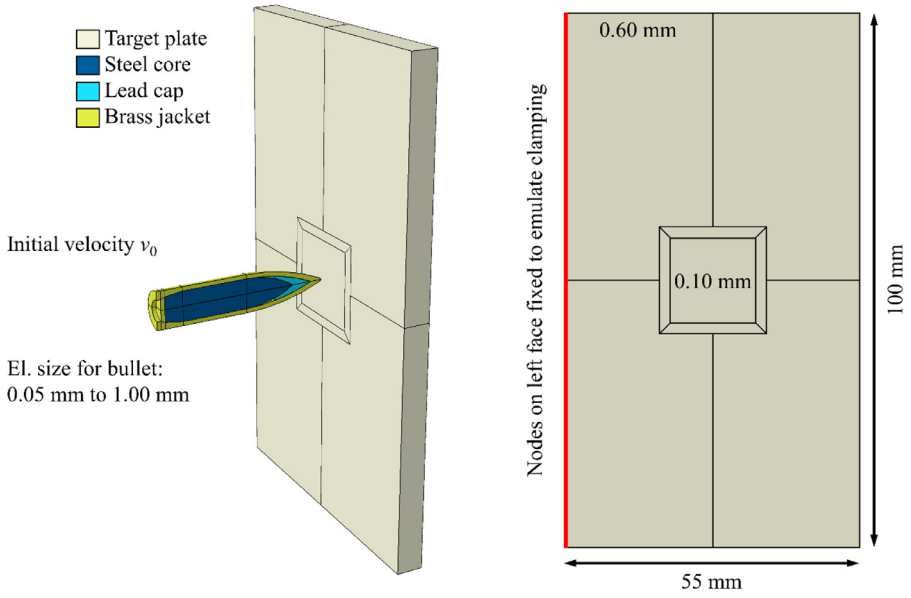

Fig. 19. Setup for the numerical simulations. The numbers specified on the target plate give the size of the solid elements in that region.

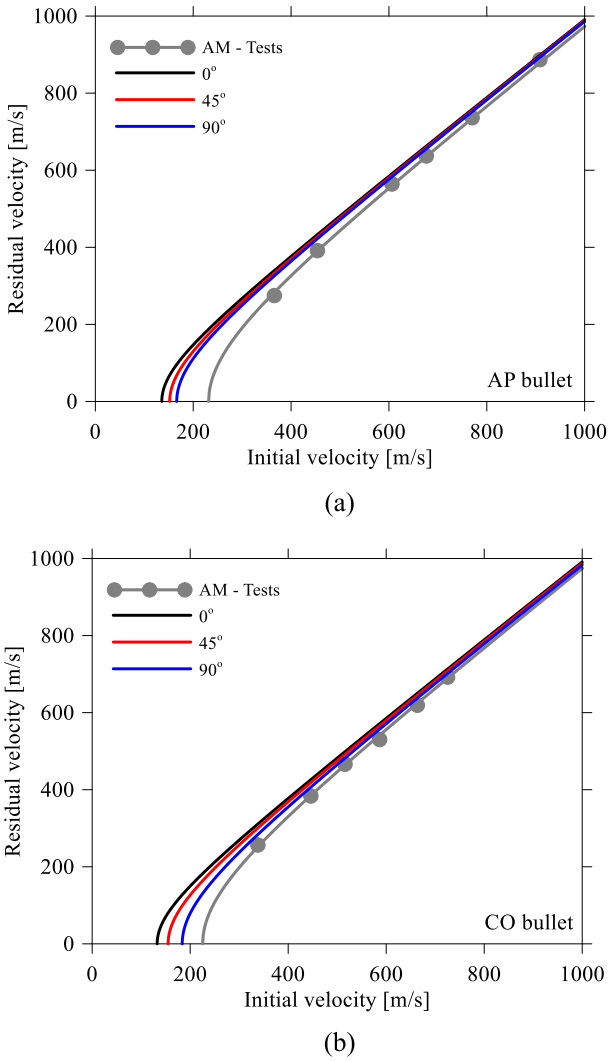

Fig. 20. Estimates for ballistic limit curves from finite element simulations of (a) AP bullets and (b) CO bullets using the three different material calibrations.

and numerically (see e.g. [1,35]).

While the failure parameters W_c of the AM material in the different calibrations seem low, especially in the built direction, decent

Fig. 22. Finite element simulation results of an AM plate perforated by three AP bullets seen from the front (top) and the side (bottom). Note that the images have been cropped to better show the details.

quantitative results are obtained. However, also the most ductile material direction, i.e., the 90° calibration, gives quite conservative estimates of the ballistic limit. This indicates that some effects are not adequately captured in the numerical model. Since no material data at elevated strain rates or temperatures are available in this study, these could be underrepresented effects in the constitutive relation. Still, the models applied here can give reasonable and conservative predictions of the ballistic behaviour of additive manufacture aluminium plates without making any modifications to the material model due to the manufacturing process.

Finally, the 3D scanned plate shown in Fig. 14 was recreated numerically. To do so, a plate model based on the 90° calibration was perforated by three AP bullets at initial velocities corresponding to the experimental values. The residual velocities were slightly higher than in the tests like already discussed (see Fig. 20(a)). The deformation profile of the simulated plate is shown in Fig. 22, which shows the same views as in Fig. 14. It is noted that the deformation corresponds well with the experiments, with smaller petals on the entry side, and larger petals with some fragmentation on the exit side. The diameter of the holes was the same as in the experiments (just below 8 mm). In general, the finite element results were satisfactory.

5.3. Cylindrical cavity expansion approximations

An alternative to time-consuming finite element simulations of the ballistic impact problem is to use an analytical approach known as the cylindrical cavity expansion theory or CCET [48–50]. In CCET, the

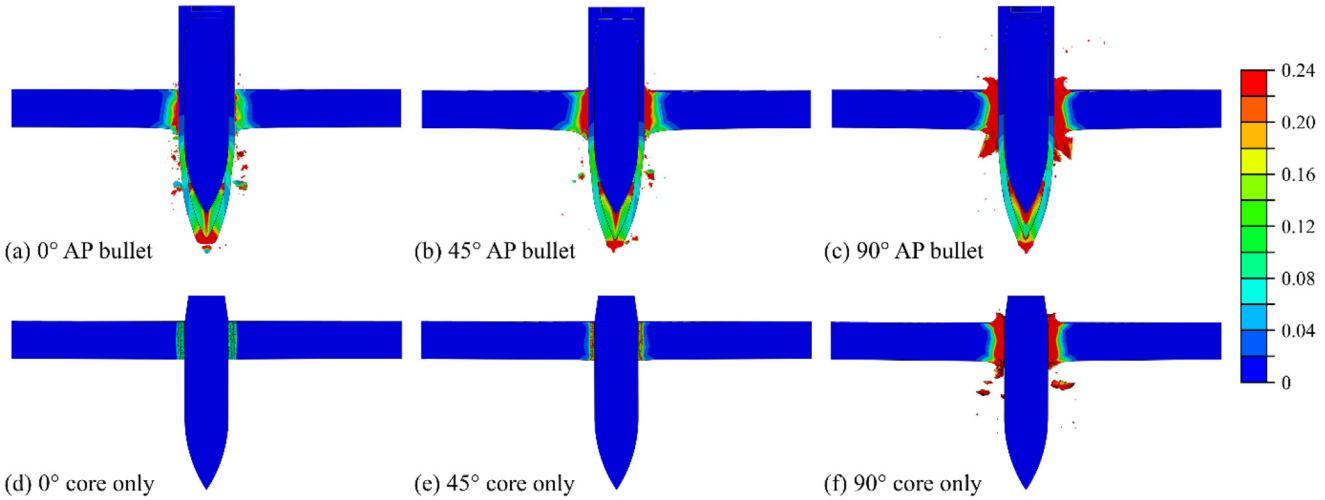

Fig. 21. Contour plots of equivalent plastic strain after 35 μs simulation time for initial velocity v_i = 700 m/s using (a) the 0° calibration, (b) the 45° calibration and (c) the 90° calibration for an AP bullet and (d) the 0° calibration, (e) the 45° calibration and (f) the 90° calibration for a CO bullet.

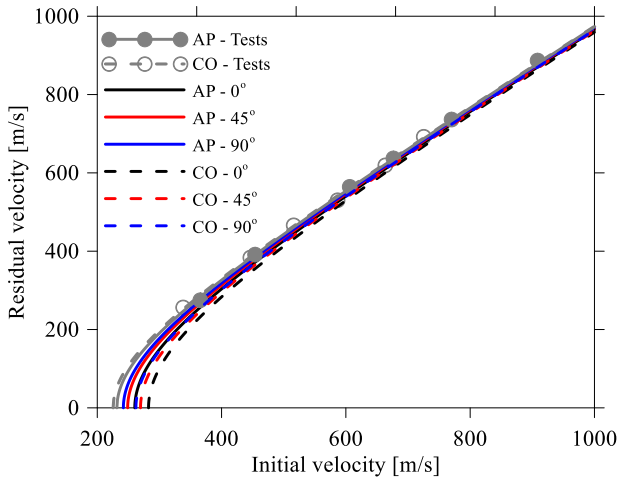

Fig. 23. Estimates of ballistic limit curves from CCET approximations with both AP and CO bullets using the three different material calibrations.

cylindrical cavity expansion solution is combined with the cylindrical cavity expansion approximation to obtain ballistic impact data such as the ballistic limit and projectile residual velocities for ductile metals perforated by a rigid striker. Even though effects like strain rate, thermal softening and friction normally are neglected in CCET, it has been found to give comparable accuracy as non-linear finite element simulations (see e.g. [51]). Recently, CCET was extended to include the Voce hardening rule in [52], and calculations have been carried out in accordance with that framework using data from Table 4. The reader is referred to [52] for a complete derivation of the CCET approach used herein.

The results from CCET calculations of both AP and CO bullets perforating an AlSi10Mg plate are shown in Fig. 23. As seen, the results are now slightly non-conservative. The reason for this is believed caused by the modest fragmentation of the plates as seen in Fig. 10, lowering the capacity somewhat [36], since CCET is derived for perforation problems where the target exhibits a perfect ductile hole growth. The CCET approximation still gives good indication of the ballistic limit at almost no computational cost and although the results are non-conservative, they are in general closer to the experimental results than the FE simulations.

6. Discussion

In this study, 5 mm thick aluminium plates of alloy AlSi10Mg were additive manufactured (AM) in a powder-bed fusion machine, before being impacted by bullets fired at various velocities from a rifle. The purpose of the study was two-fold. First, we sought to investigate if AM materials could be used in protective structures and whether their response during ballistic impact was comparable to similar but traditionally manufactured materials. Second, we wanted to investigate to what extent standard numerical and analytical techniques, frequently used in ballistic impact calculations, could be used to predict the behaviour of the AM material during penetration and perforation.

The metallurgical investigations revealed significant differences between the AM and the die-cast materials. Of particular interest with respect to the perforation resistance is that the AM material contained a number of large pores with diameter of roughly 200 μm, while the die-cast material appeared dense with only a few small pores. The difference in microstructure also affected the mechanical response, as exposed through the many uniaxial tensile tests taken from various material positions and directions. As illustrated in Figs. 6 and 7, both materials showed significant variation and anisotropy both in flow stress and strain to failure, and more so for the AM material where the strain to failure in the built direction was particularly low. It is however believed that a proper heat-treatment after printing would have reduced the anisotropic behaviour of the material [29,30].

Even though substantial differences in both microstructure and mechanical behaviour were recognized, the two materials behaved surprisingly similar during ballistic impact. The bullet perforated the materials by ductile hole growth with limited fragmentation, petals were formed on both sides of the penetration channel and the perforation process appeared ductile in a comparable way as seen in a number of similar studies on traditionally manufactured steels and aluminium alloys (e.g. [1,35]). Further, the ballistic limit curves for the AM and the die-cast materials, shown in Fig. 15 for AP bullets and in Fig. 16 for CO bullets, are almost perfectly on top of each other. It was even found that the ballistic limit velocities were slightly higher for the AM material than for the die-cast material, but the differences were marginal. In any case, these results clearly prove that for this rather low-strength material, the ballistic impact resistance is equally good for the AM material as for the traditionally manufactured die-cast material. If this conclusion also holds for AM materials like e.g. maraging steels, known for its superior strength and toughness with limited loss of ductility, and presumably a better material for ballistic protection, remains unknown and is a topic for further investigations.

Based on the experimental results, it seems reasonable that standard numerical and analytical methods should be able to predict the response of the AM material during penetration and perforation. Therefore, a much used thermoviscoplastic constitutive relation, uncoupled with an established ductile failure criterion, was calibrated using data from tensile tests on specimens extracted from various positions and directions within an AM target plate. A 3D numerical model of the impact problem was established in ABAQUS/Explicit, and finite element simulations were run using material parameter sets from the different calibrations. The results from these simulations are plotted together with the experimental data in Fig. 20 for both bullet types. As already discussed, the models were able to describe the general trends in the perforation process. They also gave decent predictions of the ballistic limit velocity without making any modifications to the material model due to the manufacturing process.

Even so, the results are more conservative than normally obtained in similar studies on traditionally manufactured materials (see e.g. [1,35]). There may be numerous reasons for this diversity, but it is believed that some are related to the lack of proper strain rate and thermal data for the AM material. Aluminium alloys are in general assumed to be rather strain rate insensitive [35], and a low strain rate sensitivity constant $C = 0.001$ was therefore applied in these simulations. It was also assumed that the flow stress drops linearly with increasing temperature, meaning that $m = 1$ was chosen. However, recent studies have indicated that printed AlSi10Mg is strain rate sensitive [18], while other studies have shown that $m > 1$ for thermally stable materials [53]. To shed some light on the effects of increased strain rate sensitivity and thermal stability on the ballistic perforation resistance of the AM material, some new simulations were run. First, a simulation applying a CO bullet with an initial velocity of 300 m/s, and $C = 0.001$ and $m = 1$ in accordance with Table 4, was run as a reference, and a residual velocity of 247.2 m/s was obtained. If these velocities are inserted into Eq. (3), assuming $a = 1$ and $p = 2$, a ballistic limit of 170 m/s is estimated. Then, simulations with $C = 0.01$ and $m = 1$ (i.e., high strain rate sensitivity), and $C = 0.001$ and $m = 2$ (i.e., high thermal stability), were run. These simulations gave residual velocities of 243.1 m/s and 242.5 m/s, resulting in estimated ballistic limits of 175.8 m/s and 176.6 m/s, respectively. Finally, a simulation with $C = 0.01$ and $m = 2$ was conducted. This simulation resulted in $v_r = 235.6$ m/s, and an estimated ballistic limit of $v_{bl} = 185.7$ m/s. In other words, by increasing C and m somewhat, the ballistic limit velocity of the material is increased by 10%. Thus, it is of utmost importance in further studies to investigate the effects of strain rate and temperature on additive manufactured protective structures to have more reliable predictions. Note finally that the possible effect of friction

between the bullet and the AM material is neglected, and it might be that friction plays a different role in this problem since Fig. 17 indicates that the penetration channel is not as smooth as seen for traditionally manufactured alloys (see e.g. [35]).

7. Concluding remarks

In this study, the ballistic perforation resistance of additive manufactured aluminium plates has been investigated both experimentally and numerically. Plates of alloy AlSi10Mg were first additive manufactured in a PBF machine. From one of these plates, material specimens were extracted at different locations and orientations before they were strained to fracture in uniaxial tension, revealing a significant scatter in both flow stress and strain to failure. Metallurgical investigations were also conducted to investigate the microstructure of the material both before and after testing. The perforation resistance of the AM plates was then examined in a ballistic range by firing APM2 bullets at various velocities towards the target plates. Both full AP bullets and only the hard core of the AP bullets were used to impact the plates. Based on high-speed camera images, the initial and residual velocities of the different bullets were measured, and the ballistic limit curves and velocities were constructed. For comparison, these studies were repeated on specimens taken from a block of traditionally die-cast AlSi10Mg having the same chemical composition as the powder used in the 3D printing. The difference in ballistic appearance between the AM and die-cast materials was negligible. Thus, the important conclusion from these tests is that an AM material may have similar or even better ballistic properties than a traditionally manufactured material with the same chemical composition. Finally, a standard material model for ballistic impact simulations was calibrated based on the material tests using inverse modelling. 3D finite element models of the ballistic tests were established in ABAQUS/Explicit, and the predicted results were compared to the experimental data. The agreement between numerical and experimental results was in general good, even though no special measures were undertaken concerning the fact that the target material was produced by additive manufacturing. All the finite element simulations gave conservative results, which is desirable from a protective point of view. For comparison, cylindrical cavity expansion approximations were used to estimate the ballistic limit at a considerably lower computational cost. Also these results were in reasonable agreement with the experimental findings, but at the non-conservative side of the experimentally obtained ballistic limit curve. Even so, a detailed investigation on the mechanical response of the AM material with respect to strain rate and temperature is required before strict conclusions can be drawn. It should finally be mentioned that a proper heat-treatment after printing could have decreased the scatter in the obtained material data and increased the ballistic limit velocity of these target plates, but that is left for further studies.

Declaration of Competing Interest

The authors declare that they have no known competing financial interests or personal relationships that could have appeared to influence the work reported in this paper.

Acknowledgement

The present work has been carried out with financial support from Centre of Advanced Structural Analysis (CASA), Centre for Research-based Innovation, at the Norwegian University of Science and Technology (NTNU) and the Research Council of Norway through project no. 237885 (CASA). The authors would like to acknowledge Mr. Trond Auestad for assistance with the various experimental programmes and Ms. Maisie Edwards-Mowforth for improving the English language.

References

[1] Børvik T, Dey S, Clausen AH. Perforation resistance of five different high-strength steel plates subjected to small-arms projectiles. Int J Impact Eng 2009;36:948–64.
[2] Ngo TD, Kashani A, Imbalzano G, Nguyen KTQ, Hui D. Additive manufacturing (3D printing): a review of materials, methods, applications and challenges. Composites Part B 2018;143:172–96.
[3] Akram J, Chalavadi P, Pal D, Stucker B. Understanding grain evolution in additive manufacturing through modelling. Addit Manuf. 2018;21:255–68.
[4] Seifi M, Salem A, Beuth J, Harrysson O, Lewandowski JJ. Overview of materials qualification needs for metal additive manufacturing. J Miner Metals Mater Soc 2016;68:747–64.
[5] Vock S, Klöden B, Kirchner A, Weissgärber T, Kieback B. Powders for powder bed fusion: a review. Prog Addit Manuf 2019:1–19.
[6] King W, Anderson A, Ferencz R, Hodge N, Kamath C, Khairallah S, Rubenchik A. Laser powder bed fusion additive manufacturing of metals; physics, computational, and materials challenges. Appl Phys Rev 2015;2:041304.
[7] Collins PC, Brice DA, Samimi P, Ghamarian I, Fraser HL. Microstructural control of additively manufactured metallic materials. Annu Rev Mater Res 2016;46:63–91.
[8] Dezfoli ARA, Hwang WS, Huang WC, Tsai TW. Determination and controlling of grain structure of metals after laser incidence: theoretical approach. Sci Rep 2017;7:41527.
[9] Daryadel S, Behroozfar A, Minary-Jolandan M. Toward control of microstructure in microscale additive manufacturing of copper using localized electrodeposition. Adv Eng Mater 2019;21:1800946.
[10] Malekipour E, El-Mounayri H. Common defects and contributing parameters in powder bed fusion AM process and their classification for online monitoring and control: a review. Int J Adv Manuf Technol 2018;95:527–50.
[11] Frazier WE. Metal additive manufacturing: a review. J Mater Eng Perform 2014;23:1917–28.
[12] Dutta B, Froes FHS. Additive manufacturing of titanium alloys. Adv Mater Res 2014;1019:19–25.
[13] Olakanmi EO, Cochrane RF, Dalgarno KW. A review on selective laser sintering/melting (SLS/SLM) of aluminium alloy powders: processing, microstructure, and properties. Prog Mater Sci 2015;74:401–77.
[14] Thijs L, Kempen K, Kruth JP, Van Humbeeck J. Fine-structured aluminium products with controllable texture by selective laser melting of pre-alloyed AlSi10Mg powder. Acta Mater 2013;61:1809–19.
[15] Buchbinder D, Meiners W, Wissenbach K, Poprawe R. Selective laser melting of aluminum die-cast alloy—correlations between process parameters, solidification conditions, and resulting mechanical properties. J Laser Appl 2015;27:S29205.
[16] Kempen K, Thijs L, Van Humbeeck J, Kruth JP. Mechanical properties of AlSi10Mg produced by selective laser melting. Phys Procedia 2012;39:439–46.
[17] Mower TM, Long MJ. Mechanical behaviour of additive manufactured, powder-bed laser-fused materials. Mater Sci Eng 2016;651:198–213.
[18] Rosenthal I, Stern A, Frage N. Strain rate sensitivity and fracture mechanism of AlSi10Mg parts produced by selective laser melting. Mater Sci Eng 2017;682:509–17.
[19] Trevisan F, Calignano F, Lorusso M, Pakkanen J, Aversa A, Ambrosio AP, Lombardi M, Fino P, Manfredi D. On the selective laser melting (SLM) of the AlSi10Mg alloy: process, microstructure, and mechanical properties. Materials (Basel) 2017;10:76.
[20] SIMULIA. ABAQUS user's manual version 2019, 2018.
[21] ISO/ASTM 52900:2015 additive manufacturing — part 1: terminology.
[22] Spierings AB, Voegtlin M, Bauer T, Wegener K. Powder flowability characterisation methodology for powder-bed-based metal additive manufacturing. Prog Addit Manuf 2016;1:9–20.
[23] Aboulkhair NT, Everitt NM, Ashcroft I, Tuck C. Reducing porosity in AlSi10Mg parts processed by selective laser melting. Addit Manuf 2014;1-4:77–86.
[24] Hovig EW, Holm HD, Sørby K. Effect of processing parameters on the relative density of AlSi10Mg processed by laser powder bed fusion. Adv Manuf Autom VIII 2018:268–76.
[25] Iturrioz A, Gil E, Petite MM, Garciandia F, Mancisidor AM, San Sebastian M. Selective laser melting of AlSi10Mg alloy: influence of heat treatment condition on mechanical properties and microstructure. Weld World 2018;62:885–92.
[26] Bagherifard S, Beretta N, Monti S, Riccio M, Bandini M, Guagliano M. On the fatigue strength enhancement of additive manufactured AlSi10Mg parts by mechanical and thermal post-processing. Mater Des 2018;145:28–41.
[27] Uzan NE, Shneck R, Yeheskel O, Frage N. Fatigue of AlSi10Mg specimens fabricated by additive manufacturing selective laser melting (AM-SLM). Mater Sci Eng 2017;704:229–37.
[28] Frodal BH, Pedersen KO, Børvik T, Hopperstad OS. Influence of pre-compression on the ductility of AA6xxx aluminium alloys. Int J Fract 2017:131–49.
[29] Brandl E, Heckenberger U, Holzinger V, Buchbinder D. Additive manufactured AlSi10Mg samples using selective laser melting (SLM): microstructure, high cycle fatigue, and fracture behaviour. Mater Des 2012;34:159–69.
[30] Hitzler L, Charles A, Öchsner A. The influence of post-heat-treatments on the tensile strength and surface hardness of selective laser melted AlSi10Mg. Defect Diffus Forum 2017;370:171–6.
[31] Dørum C, Laukli HI, Hopperstad OS, Langseth M. Structural behaviour of Al–Si die-castings: experiments and numerical simulations. Eur J Mech – A/Solids 2009;28:1–13.
[32] Børvik T, Langseth M, Hopperstad OS, Malo KA. Ballistic penetration of steel plates. Int J Impact Eng 1999;22:855–86.
[33] Børvik T, Leinum JR, Solberg JK, Hopperstad OS, Langseth M. Observations on shear plug formation in weldox 460 e steel plates impacted by blunt-nosed

projectiles. Int J Impact Eng 2001;25:553–72.
[34] Forrestal M, Børvik T, Warren T. Perforation of 7075-T651 aluminum armor plates with 7.62 mm APM2 bullets. Exp Mech 2010;50:1245–51.
[35] Holmen JK, Johnsen J, Jupp S, Hopperstad OS, Børvik T. Effects of heat treatment on the ballistic properties of AA6070 aluminium alloy. Int J Impact Eng 2013;57:119–33.
[36] Holmen JK, Johnsen J, Hopperstad OS, Børvik T. Influence of fragmentation upon the capacity of aluminum alloy plates subjected to ballistic impact. Eur J Mech – A/Solids 2016;55:221–33.
[37] Holmen JK, Solberg JK, Hopperstad OS, Børvik T. Ballistic impact of layered and case-hardened steel plates. Int J Impact Eng 2017;110:4–14.
[38] Recht RF, Ipson TW. Ballistic perforation dynamics. J Appl Mech 1963;30:384–90.
[39] Forrestal M, Børvik T, Warren T, Chen W. Perforation of 6082-T651 aluminum plates with 7.62 mm APM2 bullets at normal and oblique impacts. Exp Mech 2014;54:471–81.
[40] Holmen JK, Hopperstad OS, Børvik T, Hopperstad OS. Influence of yield-surface shape in simulation of ballistic impact. Int J Impact Eng 2017;108:136–46.
[41] Børvik T, Hopperstad OS, Berstad T, Langseth M. A computational model of viscoplasticity and ductile damage for impact and penetration. Eur J Mech– A/Solids 2001;20:685–712.
[42] Cockcroft MG, Latham DJ. Ductility and the workability of metals. J Inst Met 1968;96:33–9.
[43] Dey S, Børvik T, Hopperstad OS, Langseth M. On the influence of fracture criterion in projectile impact of steel plates. Comput Mater Sci 2006;38:176–91.
[44] LS-OPT Support Site. https://www.lsoptsupport.com/(accessed 24 September 2019).
[45] Kane A, Børvik T, Berstad T, Benallal A, Hopperstad OS. Failure criteria with unilateral conditions for simulation of plate perforation. Eur J Mech – A/Solids 2011;30:468–76.
[46] Belytschko T, Liu WK, Moran B, Elkhodary KI. Nonlinear finite elements for continua and structures. 2nd Edition John Wiley & Sons Ltd; 2014.
[47] Ruggieri C, Panontin TL, Dodds RH. Numerical modeling of ductile crack growth in 3-D using computational cell elements. Int J Fract 1996;82:67–95.
[48] Bishop RF, Hill R, Mott NF. The theory of indentation and hardness tests. Proc Phys Soc 1945;57:147–59.
[49] Hill R. The mathematical theory of plasticity. Oxford University Press; 1950.
[50] Forrestal MJ, Warren TL. Perforation equations for conical and ogival nose rigid projectiles into aluminum plate targets. Int J Impact Eng 2009;36:220–5.
[51] Børvik T, Forrestal MJ, Hopperstad OS, Warren T, Langseth M. Perforation of AA5083-H116 aluminium plates with conical-nose steel projectiles – calculations. Int J Impact Eng 2009;36:426–37.
[52] Johnsen J, Holmen JK, Warren TL, Børvik T. Cylindrical cavity expansion approximations using different constitutive models for the target material. Int J Prot Struct 2018;9:199–225.
[53] Erice B, Gálvez F, Cendón D, Sánchez-Gálvez V, Børvik T. An experimental and numerical study of ballistic impacts on a turbine casing material at varying temperatures. J Appl Mech 2011;78. 051019-1.